

Fast Nonsupervised 3-D Registration of PET and MR Images of the Brain

Jean-François Mangin^{1,2}, Vincent Frouin¹, Isabelle Bloch²,
Bernard Bendriem¹ and Jaime Lopez-Krahe²

1: Service Hospitalier Frédéric Joliot, CEA, Orsay, France

2: Télécom Paris, France

Address correspondence and reprint requests to J-F Mangin at

Service Hospitalier Frédéric Joliot

Commissariat à l'Energie Atomique

4, Place du Général Leclerc

91401 Orsay Cedex

France

tel: 33-1-69-86-77-70

Summary—We propose a fully nonsupervised methodology dedicated to the fast registration of PET and MR images of the brain. First, discrete representations of the surfaces of interest (head or brain surface) are automatically extracted from both images. Then, a shape-independent surface matching algorithm gives a rigid body transformation, which allows the transfer of information between both modalities. A 3-D extension of the chamfer matching principle makes up the core of this surface matching algorithm. The optimal transformation is inferred from the minimization of a quadratic generalized distance between discrete surfaces, taking into account between-modalities differences in the localization of the segmented surfaces. The minimization process is efficiently performed via the precomputation of a 3-D distance map. Validation studies using a dedicated brain-shaped phantom have shown that the maximum registration error was of the order of the PET pixel size (2mm) for the wide variety of tested configurations. The software is routinely used today in a clinical context by the physicians of the SHFJ (more than 150 registrations performed). The entire registration process requires about five minutes on a conventional workstation.

Index Terms—Automatic Registration, Chamfer Matching, Free-Form Surface Matching, Anisotropic Distance Map, Anatomico-Functional Correlation.

Running Title: Automatic 3-D Registration of PET and MR Images

A number of approaches to the analysis of physiological data obtained from PET require complementary anatomical information from another modality such as MRI [Mazziotta et al.: 1991]. Since scans are not (and often cannot be) performed with a perfectly reproducible patient positioning, increasing needs for accurate and reproducible 3-D registration methods have appeared. Most of the existing methods involve user interaction. Procedural approaches, which rely on specific acquisition protocols (stereotactic frames [Clarysse et al.: 1991], headholders [Bettinardi et al.: 1991], external markers [Maguire et al.: 1991, Koeppe et al.: 1991]), suffer from lack of versatility. Retrospective assisted approaches, which rely on the identification of external or internal landmarks by an expert in anatomy [Ende et al.: 1991, Bookstein: 1991, Lemoine et al.: 1991], or on interactive tools allowing a manual registration based on visual criteria [Pietrzyk et al.: 1990, Greitz et al.: 1991, Evans et al.: 1991], are more satisfactory but may suffer from lack of reproducibility. Therefore, semi-automatic retrospective methods have been proposed in order to register 3-D medical images containing a relatively rigid portion of

the human body. They may be classified into several categories according to three classical criteria: the organization level of the common features to match (basic, structured), the type of transformation used to map an image onto the other (parametric models, elastic matching), the algorithm used to match the features (local, global).

With regard to multimodality registration, conventional correlation techniques based on basic features (voxels, sets of voxels) are not adequate since the images reflect different types of information. Nevertheless, a new approach maximizing the uniformity of the PET pixel values within several partitions of the corresponding MR image has been proposed recently in [Woods et al.: 1993]. Generally, more structured features have to be extracted from the images before the registration. This can be achieved via a pre-processing step using geometric (planes, segments), topological (connected components, surfaces, surface borders), morphological (skeletons, convex hulls) or differential (ridges, parabolic lines) properties.

The nonrigidity of most anatomical structures and the complex distortions induced by the acquisition processes leads us to performing elastic registration. However, unlike the 2-D case, only few contributions to this topic have been made in 3-D [Bajcsy and Kovacic: 1989, Dann et al.: 1989, Szeliski and Lavallée: 1993]. Nevertheless, extensions of some 2-D techniques may be expected [Moshfeghi: 1991, Cohen et al.: 1992a]. Practically, parametric models of transformation (rigid body motion, affine or polynomial transformations) seem sufficient for most medical applications.

Local matching algorithms rely on the pairing of analogous features (according to characteristic properties) with a constraint of spatial coherence. One of their main interests is that they generally do not require any initialization. In [Guéziec and Ayache: 1992, Thirion et al.: 1992], 3-D curves characterizing the skull surface are used to match two CT acquisitions.

Global matching algorithms rely on the minimization of a global similarity measure. They require a good initial guess but generally provide more accurate results because the information used in the matching process is more uniformly distributed throughout the images than in the case of local approaches. Most of the contributions to the semi-automatic 3-D registration of volumetric medical images belong to the “global class”. The common feature is usually the surface of the object of interest. The similarity measure is then a generalized distance between surfaces described by point sets. This generalized distance relies on a quadratic criterion, which is constructed from a “point to surface” proximity function. The main differences between the numerous proposed approaches concern the

choice of this proximity function and the way to minimize the generalized distance (dedicated downhill search methods [Pelizzari et al.: 1989, Lavallée et al.: 1991, Brunie et al.: 1992, Mangin et al.: 1992] or a multiscale strategy [Oghabian and Todd-Pokropek: 1991] combined with a multiple starting point approach in [Jiang et al.: 1992a, Jiang et al.: 1992b]). A more detailed comparative review of the possible choices will be expounded further in this paper. A similar approach to match objects is proposed in [Malandain and Rocchisani: 1992]. The minimization relies on the simulation of the motions of one object, via the laws of dynamics, in a force field generated by the other object. In [Bloch: 1990], the common feature is the convex hull of the surface, which endows the distance to minimize with good properties. In [Steinmetz et al.: 1992], the 3-D registration is inferred from the simultaneous 2-D registration of three projections of the surfaces to match. An approach using the principal axes and the center of mass is proposed in [Alpert: 1990]. This method requires the segmentation of two identical objects to give accurate results (which is generally impossible) unless the matching is used iteratively using a “field of view box” [Arata and Dhawan: 1992]. An exhaustive review on the numerous approaches to medical image matching can be found in [Van den Elsen et al.: 1993]. A comparative study on the registration of 3-D medical images has been proposed in [Collignon et al.: 1993b]). Moreover, a recent review of 3-D registration methods for free-form 3-D shapes used in computer vision is available in [Besl and McKay: 1992]. A number of the works described in this review deal with range images, but the similarities between the shape of some of the objects used in this domain (bust sculptures) and medical objects leave the door open to fruitful collaborations [Collignon et al.: 1993a].

In this paper, we propose an approach which belongs to the global class of methods. A 3-D extension of the chamfer matching principle makes up the core of this approach. This principle consists in finding the best fit between two sets of points by minimizing a generalized distance between them, using a pre-computed distance map [Borgefors: 1988]. The edge points of one image are transformed by a parametric transformation which describes how the images can be geometrically corrected in order to perform the registration. The originality of the parametric transformation used in this paper is the combination of a classical rigid transformation with a model of the potential between-modalities differences in the localization of the surface of interest. Validations using a dedicated brain-shaped phantom show that this original feature highly improves the registration method accuracy in a multimodality context.

The surface matching algorithm constitutes the core of a fully nonsupervised PET and MRI 3-D

registration method using either the head surface (extracted from the transmission images for PET), or the brain surface (extracted from emission images for PET when the tracer is distributed throughout the whole brain). This registration technique assumes that the objects to match are rigid bodies. This assumption implies that PET and MR images have to be corrected for the various distortions induced by the image acquisition processes before the registration. In this paper, the effects of these distortions will not be addressed. We also emphasize that, in our opinion, the between-modality differences in the localization of the segmented surfaces (given by an automatic edge detection step) definitely rule out accurate scale corrections in the registration process. Therefore, we have chosen to include a correction of these localization differences in our surface matching process, assuming that the pixel sizes and the slice thicknesses yielded by the scanner calibration are accurate. Our method provides a 3-D transformation (rigid body motion) which allows information transfers between modalities by transforming volumes of interest or by resampling the image of one scan along the planes of the other.

I. METHODS

Generalized distance between surfaces

The surfaces to match are described by point sets resulting from an automatic edge detection and surface segmentation steps. The registration algorithm matches a mobile surface \mathcal{S}_{mob} coming from the PET image with a reference surface \mathcal{S}_{ref} coming from the MR image. For a position of the mobile surface described by a rotation matrix R and a translation vector T , the fit $f(R, T)$, which may be considered as a generalized distance between surfaces, is computed as follows.

1. For each point of \mathcal{S}_{mob} :
 - map the point in the MR study coordinate system;
 - if the mapped location is included in the MR field of view, compute the Euclidean distance from this location to the nearest point of \mathcal{S}_{ref} .
2. Compute the root mean square average of the distances obtained above.

3-D distance map

The use of distance maps to design accurate 3-D registration methods has recently become a topic of interest in several research laboratories [Lavallée et al: 1991, Jiang et al.: 1992a, Mangin et al.: 1992,

Malandain and Rocchisani: 1992, Collignon et al.: 1993a, Szeliski and Lavallée: 1993]. Indeed, it provides two important improvements of the initial surface matching approach of Pelizzari [Pelizzari et al.: 1989]. First, the surface matching algorithms do not depend on the surface shape. Second, \mathcal{S}_{mob} can be represented by a larger set of points which results in a better registration accuracy and in a smoother function to minimize. The principle consists in precomputing the Euclidean distance to the reference surface \mathcal{S}_{ref} for each point of the MR field of view. Thus, a discrete distance map is obtained. (see Fig.1.A). Hence, during the minimization of $f(R, T)$, the Euclidean distance from any location in the MR field of view to \mathcal{S}_{ref} is efficiently extracted from the distance map using a trilinear interpolation.

Since the computation of the distance map using an exhaustive algorithm would require a prohibitively long computation time, we use a distance transformation (DT). A DT converts a binary image consisting of object and background points into a grey level image, in which each point value corresponds to the distance from the object. Many DTs have been described in the literature (city block, chessboard, and so on). In this paper, we are only interested in the DTs that accurately approximate the Euclidean distance [Borgefors: 1984, Danielsson: 1980].

The chamfer DT is a well-known efficient DT based on the following principle. Let us consider the lattice corresponding to the image grid (the lattice nodes being the image voxels). Let us define a set \mathcal{P} of “allowed elementary displacements” in this lattice (see Fig.1.B). Let us assign to each elementary displacement \vec{p}_i of \mathcal{P} a length d_i . The set \mathcal{P} and the associated set of d_i define a chamfer mask. Let us now consider the graph whose nodes are the image voxels and whose arcs correspond to the set of elementary displacements defined by the chamfer mask. The chamfer distance between two voxels is the length of the shortest path connecting these two points in this graph (see Fig.1.B). An efficient propagation algorithm allows the fast computation of chamfer distance maps. The accuracy of the approximation of the Euclidean distance depends on the size of the mask, on the chosen elementary displacements, and on the associated lengths. Since the computation cost of the chamfer DT varies linearly with the size of the mask, a number of works have been dedicated to the design of optimal masks according to the accuracy with which the Euclidean distance is approximated [Borgefors: 1986, Verwer: 1991]. Such optimal masks assure less than 2% of maximal relative difference between chamfer distances and Euclidean distances with relatively small sets \mathcal{P} . Unfortunately, the extension of this kind of work to the case of a 3-D anisotropic image turns out to be problematic for theoretical reasons which are beyond the scope of this paper. Therefore, instead of

designing optimal 3-D chamfer masks, we use a hybrid method taking advantage of several simple chamfer masks.

Since for a registration application the accuracy of the approximation of the Euclidean distances is only required in the neighborhood of the object, we have chosen to develop an adaptive chamfer transformation. Two nested masks are used (see Fig.1.C). First, the smaller one is propagated throughout the whole lattice, yielding a rough distance map. Next, the complement of the smaller mask in the larger one is propagated in a neighborhood \mathcal{N} of the object defined from this rough distance map. The distance map is then composed of two types of values: the result of an accurate chamfer DT for the points of \mathcal{N} and the result of a rougher one elsewhere. A last refinement is performed for each point P of \mathcal{N} , using the fact that near the object, the point of the object giving the shortest path to P is, most of the time, the nearest one to P in the Euclidean sense. We precompute an equivalence table between values given by the chamfer DT and the corresponding Euclidean distances. This is done by applying this DT to a little 3-D image (whose size is bound to the definition of \mathcal{N}) using an object reduced to a single point. This table may be considered as a look-up table which allows swift correction. As a result of this last transformation, the distance map yields the exact Euclidean distance in a neighborhood of the reference surface.

Surface matching

In this section, we address the minimization of the multidimensional function f , whose global minimum defines the optimal matching between the two surfaces, over the rotation and translation parameters. This minimization is usually the most difficult step in the automatization of global matching methods. Indeed, because of the nonconvexity of the similarity measure, the minimization algorithm has to avoid potential local minima. The general way to overcome that kind of problem is to make a global heuristic (e.g. simulated annealing) manage a conventional local minimization algorithm (e.g. steepest descent). The general heuristic chosen in [Borgefors: 1988, Besl and McKay: 1992, Jiang et al.: 1992b] consists in using a multiple starting point approach and in searching down towards a local minimum for each starting point. This approach is generally combined with a multiscale minimization strategy, which speeds up the process, in order to keep reasonable computation time.

Our own experiences concerning the matching of smooth and almost convex surfaces (i.e. brain and head surface) have led us to design a simpler and more efficient dedicated heuristic yielding a very good estimation of the global minimum. This heuristic has been inferred from experimental observations about

the shape of the function to minimize (especially about the different kind of local minima which may occur). The heuristic idea consists in a downhill search of the registration parameters performed on a step by step basis with a decreasing step magnitude in order to avoid being trapped into possible small local minima (see Fig.2.A). It should be pointed out that this heuristic is conceivable provided that no scale corrections are introduced in the minimization process. Otherwise the function f might suffer from unpredictable local minima.

We now address the choice of the local minimization algorithm which will be managed by the global heuristic. Sophisticated gradient descent techniques [Lavallée et al.: 1991, Brunie et al.: 1992] are not usable since the function to minimize is not continuous (the number of points contributing to f varies with the position of \mathcal{S}_{mob}). Among the wide variety of descent methods, we have chosen the one proposed by Cox in [Cox et al.: 1989], which is dedicated to the minimization of a function of the parameters of a rigid body transformation and appears to be the most adapted to the heuristic described above. This method treats the rotation and translation parameters separately. It associates each orientation of the mobile object with the translation that minimizes f . Consequently, two nested decreasing step magnitude global heuristics can be performed, the first one being applied to the rotation parameters and the second one to the translation parameters. It should be pointed out that if we had chosen a method treating all parameters at the same level (e.g. Powell method [Pelizzari et al.: 1989]), it would have been difficult to balance the step magnitude decrease since rotation and translation parameters have a very different geometrical meaning. A more detailed description will be expounded further in the paper.

The whole surface matching process integrates two modifications of \mathcal{S}_{mob} sequentially. The first one, which is crucial in a multimodality context, consists in correcting between-modality differences in the localization of the segmented surfaces. The second one is a classical outlier elimination. Hence, the whole matching process links three searches for the optimal rigid body transformation. The first one matches the initial surfaces, the second one integrates the first modification mentioned above and the third one both modifications. The second and third minimizations are initialized by the optimal result yielded by the former minimization.

A. Initialization

A.1) Head surface matching:

The rotation angle between both acquisition orientations never exceeds 30 degrees, which assures the

convergence of our minimization process to a good estimation of the global minimum with $R_{init} = Id$, where R_{init} is the initial rotation and Id the null rotation. To get T_{init} (initial translation), we simply translate the center of mass of \mathcal{S}_{mob} so that it coincides with the center of mass of \mathcal{S}_{ref} .

A.2) Brain surface matching:

When the surface of interest is that of the brain, we perform a quick registration using the head surface, which is used to initialize a second matching process (see Fig.3). This second registration allows the correction of a possible subject motion between PET transmission and emission acquisitions. Indeed, we have noted that a rotation motion of up to 5 degrees around the axis defined by the ears is frequent and may induce large registration errors when the registration is inferred from a head surface matching.

B. Matching algorithm

B.1) Optimal rigid transformation estimation:

The minimization algorithm consists of two nested minimization levels. The high level is the search for the best rotation matrix. For each matrix R , the fit is measured as the generalized distance value yielded by the translation vector $T_{min}(R)$ which minimizes $f(R, T)$. The low level is the search of $T_{min}(R)$ for a given R . Each level of minimization is performed on a step by step basis, using a restricted number of allowed displacements in the parameter space, with a decreasing step magnitude to avoid being trapped into small local minima. This minimization algorithm is described in detail for a mono-dimensional function in Fig.2.A. The extension of this principle to multi-dimensional functions is straightforward. For the low level, the allowed displacements in the parameter space correspond to the six possible translations in the axis directions. For the high level, the allowed displacements correspond to the six possible rotations around the axes containing the center of mass of \mathcal{S}_{mob} . The general shape of the functions to minimize at each level explains the relevance of the chosen heuristic (see Fig.2.B and Fig.2.C).

B.2) Inflation of \mathcal{S}_{mob} :

We found that differences in the localization of the homologous segmented surfaces may cause registration errors. These differences result from the fact that the position of the contours produced by the edge detector (compared with the real position of the surface of the object) depends on the modality. As a result, the two detected surfaces are slightly “concentric” which induces a registration error dependent on the shape of the surface of interest. An illustration of the problem in the 2-D case is given in Fig.2.D. It should be pointed out that this localization problem, which results from a complex combination of

several parameters (tissue property imaged by the modality and hence radioactive tracer in PET, acquisition protocols, voxel geometry and edge detector characteristics), still exists when the surfaces are defined manually or extracted using a thresholding. We have overcome this problem by roughly assimilating the localization differences with a 2-D or 3-D inflation (according to the 2-D or 3-D edge detection) of \mathcal{S}_{mob} in the direction of the gradient yielded by the edge detection step. An important difference between scaling and inflation should be noted. Scaling depends on the surface shape and size. On the contrary, the effect of inflation is the same at any location in the mobile surface, which appears to be a very appealing model to correct between-modality detection differences, which should be of the same kind at any edge location.

Let R_{opt} be the rotation corresponding to the estimation of the global minimum of $f(R, T)$ found during a first minimization. We determine the size L (L being a scalar value) of the inflation that minimizes $f(R_{\text{opt}}, T_{\text{min}}^L(R_{\text{opt}}))$, where $T_{\text{min}}^L(R_{\text{opt}})$ is the translation vector that minimizes $f(R_{\text{opt}}, T)$, after a preliminary inflation of size L of \mathcal{S}_{mob} . This is achieved via a step by step algorithm similar to the one described in Fig.2.A with respect to L and the translation parameters. Finally, we perform a new minimization process including this optimal preliminary inflation of \mathcal{S}_{mob} , which refines the first optimal transformation.

We stress the importance of this kind of correction in the context of multimodality image registration. Moreover, these surface localization differences explain the difficulty of introducing relevant scale corrections in a registration method relying on surface matching.

B.3) Elimination of the outliers:

When the surface of interest is the brain surface, a last refinement is performed to account for possible segmentation differences which might induce a bias in the matching criterion (this problem may occur because of the presence of non-anatomical contours in the functional images). This classical correction consists in eliminating the outliers, i.e. the points of \mathcal{S}_{mob} which belong to contours without analogous ones in \mathcal{S}_{ref} . This is simply performed at a final stage of the matching process by introducing a threshold on the distance to \mathcal{S}_{ref} (in practice two times the global minimum of the generalized distance) which allows to eliminate the outliers from \mathcal{S}_{mob} before performing a third last minimization.

Surface representations

We now address the extraction of the surface representations. We deliberately use simple but robust processes in order to obtain a fully unsupervised method. Therefore, we deal with relatively rough

representations of the surfaces of interest which have turned out to be adequate to achieve very good registration results. Nevertheless, the introduction of sophisticated segmentation methods like active contours [Cohen et al.: 1992b, Rougon and Prêteux: 1991] generating very accurate representations is possible, provided that they could be automatically initialized.

A. Edge detection filters

We use efficient recursive and separable edge detection filters developed from Canny's ideas, followed by a classical extraction of the gradient local extrema (in the gradient direction) and a hysteresis thresholding [Canny: 1986, Deriche: 1987, Monga et al.: 1991]. The detection can be performed in 2-D or in 3-D, according to the axial sampling and resolution. It should be noted that a 3-D detection yields edges regardless of the surface orientation but at the expense of a high computation cost (see Fig.4). In practice, 3-D edge detection requires isotropic images, which are generally not available from modern scanning techniques. Consequently, the influence of the required preliminary interpolation in the localization of the 3-D edges should be questioned when the ratio between slice thickness and pixel size is large. For the results presented in this paper, since the slice thickness of the MRI data is about three times larger than the pixel size, we have performed a 2-D detection, which has turned out to be sufficient to obtain accurate registrations.

B. Surface segmentation

Robust series of processes have been designed for each modality and each surface of interest to automatically select (when it is required by the matching algorithm) the appropriate edges from the binary image of gradient extrema. It should be noted that some choices are linked to our acquisition protocols (use of a pillow during the PET acquisitions for instance) and to the geometry of the acquisitions (slice thickness, pixel size, contiguous or noncontiguous slices). Consequently, the use of our method with other acquisition protocols might require slight adjustments.

B.1) Head surface:

The head surface is simply extracted from the PET transmission edges via a 3-D connectivity criterion (which mainly eliminates the points belonging to the surface of the pillow) (see Fig.5). From MRI edges, we select the candidate edges by drawing rays from the image borders. We next eliminate the small connected components resulting from the possible presence of holes in the head surface (ears, nose) (see Fig.5).

B.2) Brain surface:

The brain surface is extracted from the PET emission edges via a 3-D connectivity criterion (see Fig.6). A few non-anatomical contours may remain in the representation (mainly at the level of the cerebellum), but we get rid of their influence on the generalized distance thanks to the outlier elimination. We emphasize that our method does not require the extraction of the brain surface from the MRI edges since the brain surface matching process is initialized from a first swift head surface matching (see Fig.3). Nevertheless, when no transmission data are available, the brain can be segmented with 3-D mathematical morphology (thresholding, 3-D erosion, selection of the largest 3-D connected component, 3-D limited conditional dilation). Unfortunately, this chain of operators is relatively expensive computationally and may require a supervisor (threshold choice, anatomical variability).

II. RESULTS

Simulations

The registration method has been first tested with sets of simulated MR images synthesized from a quasi-isotropic MR image by applying known transformations (rigid body 3-D motions, re-scalings). The goal of these simulations was to study the constraints which had to be imposed on the angle between the initial orientation of the mobile surface and the optimal orientation after registration to assure the success of the matching algorithm with head-shaped or brain-shaped surfaces of interest. We have noticed in all cases a successful matching when this angle was not exceeding 30 degrees. We think that trying to infer precise information on the accuracy of the method or even on its robustness from this kind of simulation would not be relevant. Indeed, the combined influence of a great number of parameters (slice thicknesses, location of the outliers, shape of the particular used object, orientation of the applied rotation axis, size of the surface overlap,...) can not be investigated objectively. Furthermore, simulations may lead to a large overestimation of the accuracy of the registration method, because they differ drastically from real multimodality situations, which include complex distortions of the object induced by the acquisition processes, nonrigidity of the brain or potential motions of the subject.

Experiments on real data

We have assessed the accuracy of the registration method in a real multimodality context using a rigid brain-shaped phantom. We have also checked the robustness of the non-supervised methodology with the successful registration of more than 150 clinical acquisitions.

MRI scans were performed with a MRMAX (G.E., 0.5 T magnet) and PET scans with an ECAT 953 B/31 (Siemens/CTI). The slice thickness in most of the experiments was 3.37 mm for both modalities. The pixel size was 1.03 mm for MRI and 1.96 mm for PET. The MRI volumes contained 35 to 45 slices and the PET volumes 31 slices. The algorithms have been implemented in C language on a SUN Sparcstation-II. The whole registration process was performed without supervision (see Fig.3). The mobile surfaces contained about 10 000 points and the total CPU time was about 5 min. The final quadratic average at the end of the matching process was of the order of 1 mm (about 2% of the points of \mathcal{S}_{mob} being eliminated as outliers). The size of the optimal inflation ranged from 1 to 3mm, the largest inflations being obtained for the head surface matching).

A. Phantom studies

The experimental device used was made of a 2cm thick polystyrene box in which a brain-shaped glass phantom filled with 18-fluorine was fixed. In addition, 16 test tubes filled with the same dilution were fastened to the external surface of the box (see Fig. 7). This 3-D rigid device was imaged in a fixed position with the PET scanner with different orientations of the gantry (the nine possible combinations of the gantry tilt and rotation with angles of -5° , 0° or 5° . Corresponding transmission scans were acquired the following day with the phantom still in place when the radioactivity had sufficiently decayed to allow correct measured attenuation corrections. The same device was also imaged with the MRI scanner in 3 different positions. The last one was performed with a smaller slice thickness than the previous ones (2mm versus 3.375mm) in order to test the influence of this parameter. We have noticed afterwards that a large air bubble had entered the phantom through a glass fissure before the last MRI acquisition. Making use of this incident, we were able to test the method when the surfaces of interest did not fully overlap, which may occur in some pathological cases.

Each 3-D PET image has been registered with each 3-D MR image first using our method and the phantom surface and second using a classical landmark-based method matching the centers of gravity of the 16 test tube contents as landmarks. This landmark-based method, which is known as the Procrustes algorithm, finds the optimal rigid transformation (in a least-squares approach) which fits two corresponding 3-D point sets [Arun et al.: 1987]. Using simulations of perfectly rigid objects, Evans et al. have shown that with a 3-D Gaussian error model for the localization of the landmarks (standard deviation σ), the residual error after registration by this method with 15 landmarks can be assessed as 0.1σ [Evans et al.: 1989].

Consequently, since our landmarks are well defined (the test tube contents are automatically extracted from the images using connectivity properties), we can assume a very good accuracy for the registration results yielded by this method. Therefore, the results of this landmark-based method can be used as a “gold standard” to validate our registration method. Indeed, this results yield a point to point pairing between the PET and MR acquisitions. Using this “gold standard” rather than a straight comparison using only the landmark locations results in two important improvements. First, the influence of the between-modality uncertainty on the landmark locations is statistically reduced by the RMS approach. Second, the registration error can be assessed for any point of the brain phantom rather than at the level of the external landmarks. It should be noted that when the Procrustes algorithm is used in a clinical context with user specified internal landmarks, its results can no longer be considered as a “gold standard” (usually, the number of well-defined landmarks in the functional images is low).

Registration methods versus PET gantry controller

We propose first to assess separately the accuracy of both registration approaches using the information yielded by the PET gantry controller. The results of this study will confirm that the landmark-based method yields registration results which have to be considered as a “gold standard” in our validation. Since we do not know the center of rotation of the gantry, these results only concern the angular data. Let us choose one of the MR acquisitions. Let R_i^L (respectively R_i^S) be the rotation matrix of transformation which register this MR image with the PET image i ($1 \leq i \leq 9$) according to the landmark-based method (resp. our surface-based method). Let us consider now a couple of PET images (i, j) (with $i < j$). The PET scanner gantry rotational motion between PET acquisition i and j can be assessed from R_i^L and R_j^L by the product $R_i^L R_j^{L-1}$ (respectively from R_i^S and R_j^S by the product $R_i^S R_j^{S-1}$). Let β_{ij}^L (resp. β_{ij}^S) be the residual angle between the gantry motion value assessed with this method and the motion value inferred from the scanner controller information. β_{ij}^L (resp. β_{ij}^S) is a good measurement of the landmark-based (resp. surface-based) registration method rotational accuracy. It should be noted that this residual angle results from the complex combination of two angular registration errors (which may cancel each other out in some configurations) and of the uncertainty on the values yielded by the controller (the scanner reports angles to the nearest 0.1°). Consequently, it has to be used statistically. For one chosen MR image, the two residual angles are computed for each of the 36 possible couples (i, j) and their respective mean and maximum values are considered as measurements of the accuracy of the corresponding registration

method.

Surface-based method versus the “gold standard”

To compare the registration results of both approaches, several measurements are considered. First the residual rotation angle θ between the rotations yielded by the two methods is used to measure the registration difference as far as orientation is concerned. To measure the registration difference for a particular point M of the brain phantom located in the MR acquisition, we use the distance d_M between the two corresponding points in the PET acquisition according to each registration approach. We perform this measurement for the center of gravity of the phantom (d_G). We compute also this distance mean value, standard deviation and maximum for all points of the phantom (d_V^{mean} , $\sigma(d_V)$ and d_V^{max}) and for the points of the phantom surface (d_S^{mean} , $\sigma(d_S)$ and d_S^{max}).

Results

Table 1 displays the various measurements mentioned above taking into account the 18 (2x9) registrations performed with the first two MR images (slice thickness = 3.375mm). The rotation angle retrieved by the registration ranges from 3° to 19° . The β_{ij} behavior is displayed in Table 1.A for both approaches (β^S : surface matching, β^L : landmark-based, using the same set of registrations (2x36 couples (i, j)). Considering the uncertainty on the gantry tilt value, both methods appear very accurate, with a slight advantage for the landmark-based method. Considering $\beta^L = 0.24^\circ$ and the fact that this measure includes four values reported by the gantry controller to the nearest 0.1° (two tilts and two rotations), we have the confirmation that the landmark-based method can be regarded as a “gold standard” in the following method comparison. Table 1.B displays the result of this comparison. For each measurement (θ , d_V^{mean} , $\sigma(d_V)$, d_V^{max} , d_S^{mean} , $\sigma(d_S)$ and d_S^{max}), mean value, standard deviation and maximum are displayed. The accuracy of our method compared with the landmark-based method turns out to be lower than the PET pixel size for most of the points: for the whole imaged brain volume, $mean(d_V^{mean}) + mean(\sigma(d_V)) = 1.58\text{mm}$ as compared with a 1.956mm PET pixel size. If we consider the worst potential situation where the maximum error resulting from the landmark-based method (assessed as less than 1mm) and the maximum difference between both methods ($max(d_V^{max}) = 2.38\text{mm}$) are added to each other, the resulting error remains of the order of the PET slice thickness. A more reasonable assessment of the registration accuracy in view of $mean(d_V^{mean}) = 1.19\text{mm}$, and of the high accuracy of the landmark-based method would be the PET pixel size: 2mm (indeed, there is no reason for both registration errors to add each other).

In order to show the registration accuracy improvements induced by the modifications of the mobile surface representation performed during the matching process, Table 1.C displays the registration method comparison at different stages of the matching process: before the inflation, before the outlier elimination and at the end of the process. The various measurements displayed prove the crucial importance of both refinements in the matching process: for instance, d_V^{mean} decreases from 2.13mm with the initial mobile surface representation to 1.36mm after the inflation and to 1.19mm after the outlier elimination.

Table 2 displays the same measurements as Tables 1.A and 1.B for the 9 registrations concerning the MR image with the air bubble and the 2mm slice thickness. It has to be noted that the lower slice thickness for the reference image slightly improves the accuracy of the surface-based registration method in spite of the air bubble: $mean(d_V^{mean} = 0.97mm)$ to be compared with 1.19mm. Nevertheless, the presence of this air bubble increases the dispersion of the results: for instance, $\sigma(\theta) = 0.53^\circ$ as compared with 0.19° .

B. Studies with clinical data

An illustration of the nonsupervised registration methodology is shown in Figures 5 and 6. The robustness of this approach has been proved by more than 150 successful registrations of clinical data sets. The tracer used in a number of the functional acquisitions was the 18-fluoro-deoxy-glucose (FDG) which yielded images relatively rich in anatomical information. The registration results have been validated by physicians expert in neurology using interactive visualization tools. Considering well-defined structures of the brain (e.g. cortical rim, basal ganglia, thalamic nuclei, cerebellum), the functional information has turned out to be in accord with the paired anatomical information in all cases (see Fig. 8). As a result of these studies, the registration accuracy has been considered as highly sufficient with regard to the underlying functional studies.

III. DISCUSSION

Distance maps

The use of distance maps to design accurate 3-D registration methods appears to be a very good solution to the global surface matching problem. It allows the efficient computation of a shape-independent matching criterion relying on the Euclidean distance from a point to a surface. Hence, the method can be applied to any kind of relatively rigid object (head, vertebra, brain) or even to a set of objects (brain and ventricles for instance). Consequently, the main drawback of the widely used method of Pelizzari

[Pelizzari et al.: 1989], which uses a distance estimation relying on the relatively spherical shape of the head, can be overcome.

Anisotropic lattice

The computation of the distance map for an anisotropic lattice with an adaptive strategy is an original aspect of the work presented in this paper. An alternative could have been the change from an anisotropic lattice to an isotropic lattice, in order to use classical isotropic DT [Jiang et al.: 1992b]. Unfortunately, this change is problematic. On the one hand, the classical interpolation of the gray values in the slices may lead to artifacts in the edge detection when the ratio of slice thickness to pixel size is large. On the other hand, shape based interpolation (SBI) [Raya and Udupa: 1990, Herman and Bucholtz: 1991] is not adapted to our registration strategy. Indeed, SBI requires the segmentation of the volumetric object of interest in order to use 2-D maps of the signed distance to the border of the object in the interpolation process. First, this would imply cumbersome postprocessing of our edge images when the object of interest is the head (first matching), because \mathcal{S}_{ref} may contain “topological holes” and hence is not the border of a volumetric object. Second, when the distance map is computed from all MRI edges (brain surface matching), SBI does not seem feasible. Another interesting adaptive chamfer DT, the octree spline, has been introduced in [Lavallée et al.: 1991, Szeliski and Lavallée: 1993] as a very good trade-off between memory space, accuracy and speed of computation. The intuitive idea behind this geometrical representation is to have more detailed information (i.e. more accuracy) near the object than far away from it. Our general method could be easily adapted to this kind of DT if the size of the distance maps produced by the chamfer DT exceeds the computer capacity.

Between-modality surface localization differences

Another feature of our method is the correction of the registration error induced by between-modality differences in the localization of the surfaces to match. It constitutes an important improvement in a multi-modality context. It should be noted that although this correction is performed during the surface matching via a inflation of \mathcal{S}_{mob} , no scale correction parameter is introduced in the registration.

Generalized distance minimization

We also propose a dedicated minimization heuristic more efficient than the general multiple starting point strategy used in [Jiang et al.: 1992b]. It should be noted that this heuristic could be combined with the “growing hat” acceleration proposed in [Collignon et al.: 1993a] in order to speed up the process.

This idea consists in selecting a small number of points from the exhaustive representation of \mathcal{S}_{mob} to compute f at the beginning of the minimization, and in making it grow as the minimization advances. Nevertheless, in our opinion, trying to speed up the minimization process has to be made keeping in mind the computational cost of the segmentation process and the real needs of the user. Indeed, the interest of performing the minimization in a few seconds is poor if the segmentation of the surfaces of interest or the precomputation of a distance map take several minutes. Consequently, a minimization computation cost of the same order as the segmentation computation cost seems reasonable. Furthermore, we do not address the registration problems linked to a surgical application, which may involve a real time constraint [Lavallée et al: 1991, Brunie et al.: 1992]. In fact, a classical application of the registration of PET and MRI data can tolerate a preliminary computation time of 5 to 10 minutes. Indeed, from our collaboration with clinical researchers, it appears that the relevant issue is the robustness rather than the computation time.

Registration accuracy

Assessing the accuracy of a registration method with regard to clinical data is a real problem with often non-fully satisfactory solutions. Studying simulations provides a good idea of how the method behaves, but the results cannot be directly extended to the real cases. It should be noted that the minimum generalized distance provided by our matching algorithm does not reflect the quality of the registration, since the optimal position of \mathcal{S}_{mob} does not rely on a point to point pairing. A more satisfactory approach to assess the registration accuracy would be to use an a priori better registration technique as a “gold standard”, e.g. a head-mounted stereotactic frame, to compare the registration results [Neelin et al.: 1993]. We have applied this comparative approach using a brain-shaped rigid phantom to assess the accuracy of our method in the ideal case of a rigid object. We have shown that this accuracy is smaller than the PET pixel size. In our opinion, trying to estimate this accuracy with clinical data is nearly impossible. Indeed, we think that none of the registration techniques proposed to date is able to take into account the nonrigidity of the medical objects. Moreover the registration problem in a clinical context has no exact solution because of the potential motions or deformations of the brain during the acquisitions. This problem seems to be particularly worrying since the acquisition times are often of the order of twenty minutes for the modalities of interest in this paper. The influence, for instance, of the regular motion of the brain in the skull corresponding to every heartbeat or of some imperceptible motions of the head

(around the axis defined by the ears for instance), appears almost impossible to assess and varies with the acquisitions. Using a stereotactic frame might greatly reduce the problem of the potential motions of the subject and hence yield a good way to assess the registration accuracy, but would not overcome the problem of the nonrigidity of the brain.

Finally, whatever the registration method used, it would not be reasonable to assert that the registration accuracy is widely smaller than the scanner voxel sizes as long as the method searches for a rigid body transformation. Therefore, using a similar approach in stereotactic neurosurgery to register CT and MR images for instance, could require the extension of the method to a more complex parametric model of transformation or even to elastic matching [Szeliski and Lavallée: 1993].

Nonsupervised registration methodology

We would like to emphasize that our matching algorithm has been integrated in a fully nonsupervised registration process dedicated to PET and MRI correlation. Although the registration is inferred from a brain surface matching (when it can be detected in the PET emission image), the cumbersome segmentation of the brain in the MRI images is not required, thanks to the initialization provided by a preliminary quick registration using the PET transmission images (see Fig.5). The software is routinely used today by the physicians of the SHFJ and performs the whole registration process automatically in a few minutes (more than 150 registrations have been performed). The robustness of the method has allowed also the design of batch operations to correct patient movements during PET dynamic studies (the registration with the MR image is performed frame by frame).

IV. REFERENCES

- [Alpert: 1990] Alpert NM, Bradshaw JF, Kennedy D, Correia JA (1990) The principal axes transformation – a method for image registration. *J. Nucl. Med.* 31(10):1717–1722
- [Arata and Dhawan: 1992] Arata LK, Dhawan AP (1992) Iterative principal axes registration: A new algorithm for retrospective correlation of MRI-PET brain images. In: *14th IEEE Engineering in Medicine and Biology Society Conference*, Paris, pp. 2776–2778
- [Arun et al.: 1987] Arun KS, Huang TS, Blodstein SD (1987) Least-square fitting of two 3-D point sets. *IEEE Trans. Pattern Anal. Machine Intell.* 9(5):207–209
- [Bajcsy and Kovacic: 1989] Bajcsy R, Kovacic S (1989) Multiresolution elastic matching. *Comput. Vision, Graph. Image Processing* 46:1–21
- [Besl and McKay: 1992] Besl PJ, McKay ND (1992) A method for the registration of 3-D shapes. *IEEE Trans. Pattern Anal. Machine Intell.* 14(2):239–256
- [Bettinardi et al.: 1991] Bettinardi V, Scardaoni R, Gilardi MC, Rizzo G, Perani D, Paulesu E, Striano G, Triulzi F, Fazio F (1991) Head holder for PET, CT, and MR studies. *J. Comp. Assist. Tomog.* 15(5):886–892, 1991.
- [Bloch: 1990] Bloch. I (1990) *3-D Pattern recognition, application to chemical molecules*, Ph.D. thesis, Télécom Paris, France, N^o 90E018
- [Bookstein: 1991] Bookstein FL (1991) Thin plate splines and the atlas problem for biomedical images. In: *12th. Int. Conf. on Info. Proces. Medical Imaging*, UK, pp. 327–342
- [Borgefors: 1984] Borgefors G (1984) Distance transformations in arbitrary dimensions. *Comput. Vision, Graph. Image Processing* 27:321–345
- [Borgefors: 1986] Borgefors G (1986) Distance transformations in digital images. *Comput. Vision, Graph. Image Processing* 34:344–371
- [Borgefors: 1988] Borgefors G (1988) Hierarchical chamfer matching: a parametric edge matching algorithm. *IEEE Trans. Pattern Anal. Machine Intell.* 10(6):849–864
- [Brunie et al.: 1992] Brunie L, Lavallée S, Szeliski R (1992) Using force field derived from 3D distance maps for inferring the attitude of a 3D rigid object. In: *2nd. ECCV*, Santa Margherita Ligure, Italy, pp. 670–675
- [Canny: 1986] Canny J (1986) A computational approach to edge detection. *IEEE Trans. Pattern Anal. Machine Intell.* 8(6):679–698

- [Clarysse et al.: 1991] Clarysse P, Gibon D, Rousseau J, Blond S, Vasseur C, Marchandise X (1991) A computer-assisted system for 3-D frameless localization in stereotaxic MRI. *IEEE Trans. Med. Imaging* 10(4):523–529
- [Cohen et al.: 1992a] Cohen I, Ayache N, Sulger P (1992) Tracking points on deformable objects using curvature information. In: *2nd. ECCV*, Santa Margherita Ligure, Italy, pp. 458–466
- [Cohen et al.: 1992b] Cohen I, Cohen L, Ayache N (1992) Using deformable surfaces to segment 3-D images and infer differential structures. *Comput. Vision, Graph. Image Processing* 56(2):242–263
- [Collignon et al.: 1993a] Collignon A, Géraud T, Vandermeulen D, Suetens P, Marchal G (1993) New high-performance 3D registration algorithms for 3D medical images. In: *SPIE Medical Imaging VII, Vol. 1898*, Newport Beach, USA, in press
- [Collignon et al.: 1993b] Collignon A, Vandermeulen D, Suetens P, Marchal G (1993) Surface based registration of 3D medical images. In *SPIE Medical Imaging VII, Vol. 1898*, Newport Beach, USA, in press
- [Cox et al.: 1989] Cox P, Maître H, Minoux M, Ribeiro C (1989) Optimal matching of convex polygons. *Pattern Recognition Letters* 9:327–334
- [Danielsson: 1980] Danielsson PE (1980) Euclidean distance mapping. *Comput. Vision, Graph. Image Processing* 14:227–248
- [Dann et al.: 1989] Dann R, Hoford J, Kovacic S (1989) Evaluation of elastic matching system for anatomic (CT, MR) and functional (PET) cerebral images. *J. Comp. Assist. Tomog.* 13(4):603–611
- [Deriche: 1987] Deriche R (1987) Using canny’s criteria to derive a recursively implemented optimal edge detector. *Int. Journal of Computer Vision* 1(2):167–187
- [Ende et al.: 1991] Ende G, Treuer H, Boesecke R (1991) Optimization and evaluation of landmark-based image correlation. *Phys. Med. Biol.* 37(1):261–271
- [Evans et al.: 1989] Evans AC, Marrett S, Collins L, Peters TM (1989) Anatomical-functional correlative analysis of the human brain using three dimensional imaging system. In: *SPIE Medical Imaging III: Image Processing*, pp. 264–274
- [Evans et al.: 1991] Evans AC, Marrett S, Torrescorzo J, Ku S, Collins L (1991) MRI-PET correlation in three dimensions using a volume-of-interest (VOI) atlas. *J. Cereb. Blood Flow Metab.* 11:A69–A78
- [Greitz et al.: 1991] Greitz T, Bohm C, Holte S, Eriksson L (1991) A computerized brain atlas: Construction, anatomical content, and some applications. *J. Comp. Assist. Tomog.* 15(1):26–38
- [Guéziec and Ayache: 1992] Guéziec A, Ayache N (1992) Smoothing and matching of 3-D space curves. in: *2nd. ECCV*, Santa Margherita Ligure, Italy, pp. 620–629

- [Herman and Bucholtz: 1991] Herman GT, Bucholtz CA (1991) Shape-based interpolation using chamfer distance. In: *12th. Int. Conf. on Info. Proces. Medical Imaging*, UK, pp. 314–325
- [Jiang et al.: 1992a] Jiang H, Holton K, Robb RA (1992) Image registration of multimodality 3-D medical images by chamfer matching. In: *SPIE Biom. Image Proces. and Three-Dimensional Microscopy*, pp. 356–366
- [Jiang et al.: 1992b] Jiang H, Robb RA, Holton KS (1992) A new approach to 3-D registration of multimodality medical images by surface matching. In *SPIE Visualization in Biomedical Computing*, pp. 196–213
- [Koeppel et al.: 1991] Koeppel RA, Holthoff VA, Frey KA, Kilbourn MR, Kuhl DE (1991) Compartmental analysis of (C^{11}) flumazenil kinetics for the estimation of ligand transport rate and receptor distribution using positron emission tomography. *J. Cereb. Blood Flow Metab.* 11:735–744
- [Lavallée et al.: 1991] Lavallée S, Szeliski R, Brunie L (1991) Matching 3D smooth surfaces with their 2D projections using 3D distance maps. In: *SPIE Geometric Methods in Computer Vision*, pp. 322–336
- [Lemoine et al.: 1991] Lemoine D, Barillot C, Gibaud B, Pasqualini E (1991) A 3D C^1 stereotactic deformation model to merge multimodality images and atlas data. In: *Comp. Assist. Radiology*, pp: 662–668
- [Maguire et al.: 1991] Maguire GQ, Noz ME, Rusinek H, Jaeger J, Kramer EL, Sanger JJ, Smith G (1991) Graphics applied to medical image registration. *IEEE Computer Graphics & Applications* 11(2):20–28
- [Malandain and Rocchisani: 1992] Malandain G, Rocchisani JM (1992) Registration of 3D medical images using a mechanical based method. In: *14th Int. Conf. IEEE EMBS, Sat. Symp. on 3D Advanced Image Processing in Medicine*, Rennes, pp. 91–95
- [Mangin et al.: 1992] Mangin JF, Frouin V, Bendriem B (1992) Nonsupervised 3D registration of PET and MRI data using chamfer matching. In: *IEEE Medical Imaging Conf., with Nuclear Science Symposium, Orlando, USA*, pp. 1262–1264
- [Mazziotta et al.: 1991] Mazziotta JC, Pelizzari CC, Chen GT, Bookstein FL, Valentino D (1991) Region of interest issues: the relationship between structure and function in the brain. *J. Cereb. Blood Flow Metab.* 11:A51–A56
- [Monga et al.: 1991] Monga O, Deriche R, Rocchisani JM (1991) 3D edge detection using recursive filtering: Application to scanner images. *Comput. Vision, Graph. Image Processing* 53(1):76–87
- [Moshfeghi: 1991] Moshfeghi M (1991) Elastic matching of multimodality medical images. *Comput. Vision, Graph. Image Processing* 53(3):271–282
- [Neelin et al.: 1993] Neelin P, Crossman J, Hawkes DJ, Ma Y, Evans AC (1993) Evaluation of MRI/PET registration using simulated PET brain images. *Comput. Medical Imag. Graph.* 17(4/5):351–356

- [Oghabian and Todd-Pokropek: 1991] Oghabian MA, Todd-Pokropek A (1991) Registration of brain images by a Multi-Resolution sequential method. In: *12th. Int. Conf. on Info. Proces. Medical Imaging*, UK, pp. 165–174
- [Pelizzari et al.: 1989] Pelizzari CA, Chen GTY, Spelbring DR, Weichselbaum RR, Chen CT (1989) Accurate three-dimensional registration of CT, PET, and/or MR images of the brain. *J. Comp. Assist. Tomog.* 13(1):20–26
- [Pietrzyk et al.: 1990] Pietrzyk U, Herholz K, Heis WD (1990) Three-dimensional alignment of functional and morphological tomograms. *J. Comp. Assist. Tomog.* 14(1):51–59
- [Raya and Udupa: 1990] Raya SP, Udupa JK (1990) Shape-based interpolation of multidimensional objects. *IEEE Trans. on Medical Imaging* 9(1):32–42
- [Rougon and Prêteux: 1991] Rougon N, Prêteux F (1991) Deformable markers: Mathematical morphology for active contour model control. In: *Int. Symp. on Optical Applied Science and Engineering*, San Diego, pp. 78–89
- [Steinmetz et al.: 1992] Steinmetz H, Huang Y, Seitz RJ, Knorr U, Schlaug G, Herzog H, Hackländer T, Freund HJ. (1992) Individual integration of positron emission tomography and High-Resolution magnetic resonance imaging. *J. Cereb. Blood Flow Metab.* 12(9):919–926
- [Szeliski and Lavallée: 1993] Szeliski R, Lavallée S (1993) Matching 3-D Anatomical Surfaces with Non-Rigid Deformations Using Octree-Splines. In: *SPIE Geometric Methods in Computer Vision II*, San Diego, pp. 306–315
- [Thirion et al.: 1992] Thirion JP, Gourdon A, Monga O, Guézic A, Ayache N. (1992) Fully automatic registration of 3D CAT-Scan images using crest lines. In: *14th Int. Conf. IEEE EMBS, Paris*, pp. 1888–1890
- [Van den Elsen et al.: 1993] Van den Elsen PA, Pol EJD, Viergever MA (1992) Medical image matching: A review with classification. *IEEE Engineering in Medicine and Biology* 12(1):26–38
- [Verwer: 1991] Verwer BJH (1991) Local distances for distance transformations in two or three dimensions. *Pattern Recognition Letters* 12:671–682
- [Woods et al.: 1993] Woods RP, Mazziotta JC, Cherry SR (1993) MRI-PET Registration with Automated Algorithm. *J. Comp. Assist. Tomog.* 17(4):536–546

Table 1: **Phantom studies (MRI with a 3.375mm slice thickness)**

	β^L	β^S
	(deg.)	(deg.)
mean	0.24°	0.33°
sigma	0.13°	0.19°
max.	0.52°	0.71°

	θ	d_G	d_V^{mean}	$\sigma(d_V)$	d_V^{max}	d_S^{mean}	$\sigma(d_S)$	d_S^{max}
	(deg.)	(mm.)	(mm.)	(mm.)	(mm.)	(mm.)	(mm.)	(mm.)
mean	0.83°	1.08	1.19	0.37	1.96	1.24	0.43	1.93
sigma	0.19°	0.12	0.12	0.07	0.23	0.13	0.08	0.22
max.	1.17°	1.30	1.37	0.50	2.38	1.47	0.59	2.34

modification of \mathcal{S}_{mob}	θ	d_G	d_V^{mean}	$\sigma(d_V)$	d_V^{max}	d_S^{mean}	$\sigma(d_S)$	d_S^{max}
	(deg.)	(mm.)	(mm.)	(mm.)	(mm.)	(mm.)	(mm.)	(mm.)
no correction	2.65°	1.23	2.13	0.93	4.18	2.45	0.96	4.04
inflation	1.24°	1.11	1.36	0.53	2.45	1.46	0.58	2.40
inf. and outlier elimination	0.83°	1.08	1.19	0.37	1.96	1.24	0.43	1.93

A: Angular error in the estimation of the gantry orientation (statistical results over 72 registration couples, β^L : landmark-based method, β^S : surface-based method). **B:** Registration method comparison: angular difference in degrees (θ) and registration differences (in mm.) at the level of the center of gravity of the brain (d_G), for the whole brain volume (mean, standard deviation and maximum of d_V) and at the level of the brain surface (mean, standard deviation and maximum of d_S). For each measurement, mean value, standard deviation and maximum are displayed (statistical results over 18 registrations). **C:** Registration accuracy improvement induced by the modifications of the mobile surface representation during the matching process: The mean values of the various measurements displayed in Table 1.B are computed at different stages of the matching process: before the inflation, before the outlier elimination, at the final stage (statistical results over 18 registrations).

Table 2: Phantom studies (MRI with a 2mm slice thickness and a large air bubble):

	β^L	β^S
	(deg.)	(deg.)
mean	0.25°	0.48°
sigma	0.13°	0.25°
max.	0.51°	0.82°

	θ	d_G	d_V^{mean}	$\sigma(d_V)$	d_V^{max}	d_S^{mean}	$\sigma(d_S)$	d_S^{max}
	(deg.)	(mm.)	(mm.)	(mm.)	(mm.)	(mm.)	(mm.)	(mm.)
mean	0.97°	0.72	0.97	0.37	1.81	1.10	0.41	1.77
sigma	0.53°	0.22	0.24	0.12	0.56	0.37	0.09	0.53
max.	1.28°	0.88	1.13	0.46	2.18	1.32	0.49	2.14

Same presentation as in Table 1.A (statistical results over 36 couples) and in Table 1.B (statistical results over 9 registrations).

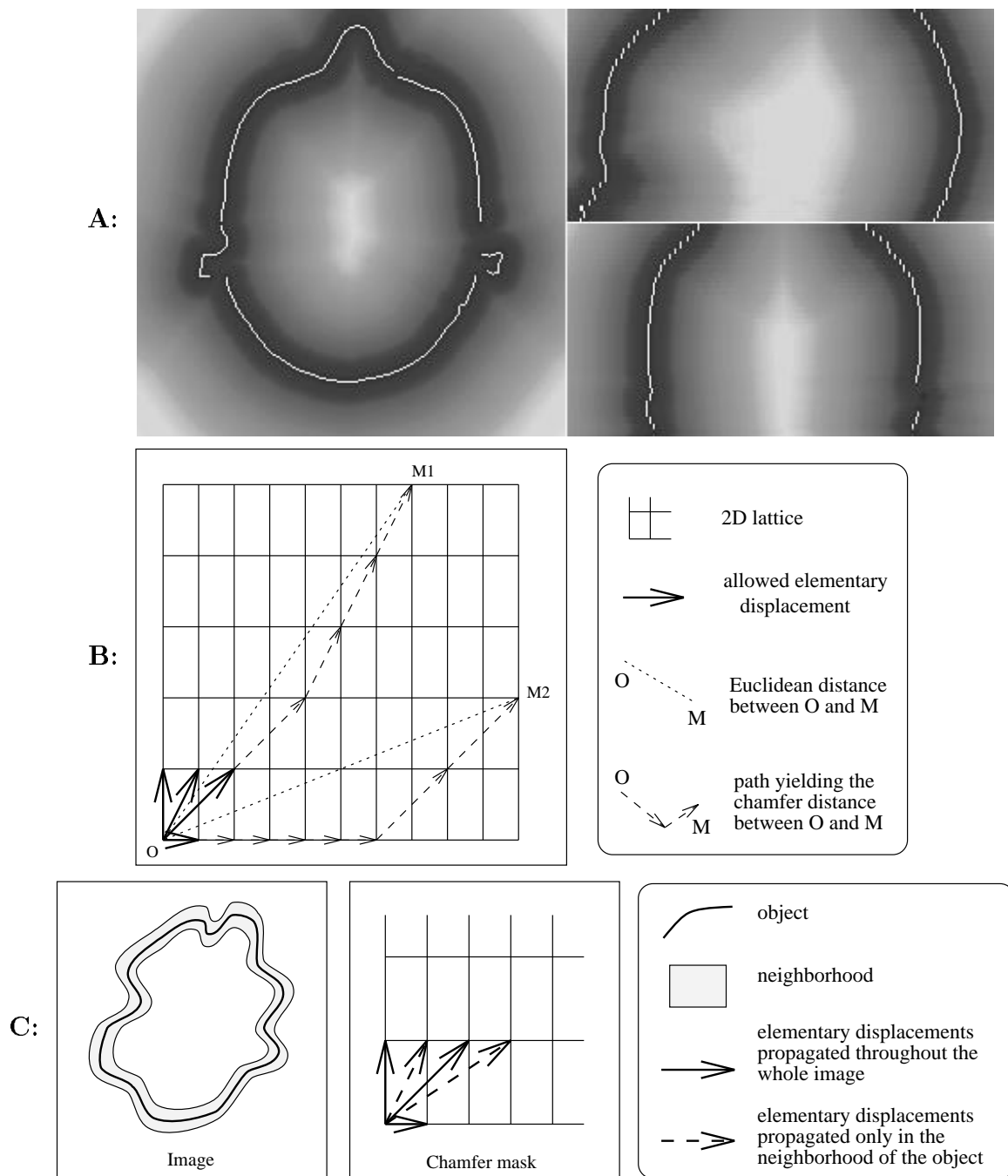


Figure 1:

A: Precomputation of a 3-D distance map to the MRI head surface (left: axial view, top-right: sagittal view, down-right: coronal view).

B: Chamfer transformation on a 2-D anisotropic lattice: The elementary displacements allowed by the chamfer mask in a quarter of the range of possible orientations are displayed. The set of allowed elementary displacements spanning the whole range ($[0, 360 \text{ deg}]$) can be inferred from symmetries. Each elementary displacement is associated with an integer (displacement length) which approximates the Euclidean length of the displacement multiplied by a scale factor.

C: Adaptive chamfer transformation in a 2-D anisotropic image: A larger set of elementary displacements is used near the object which results in a better approximation of the Euclidean distance. This adaptive approach minimizes the computation cost of the distance transformation.

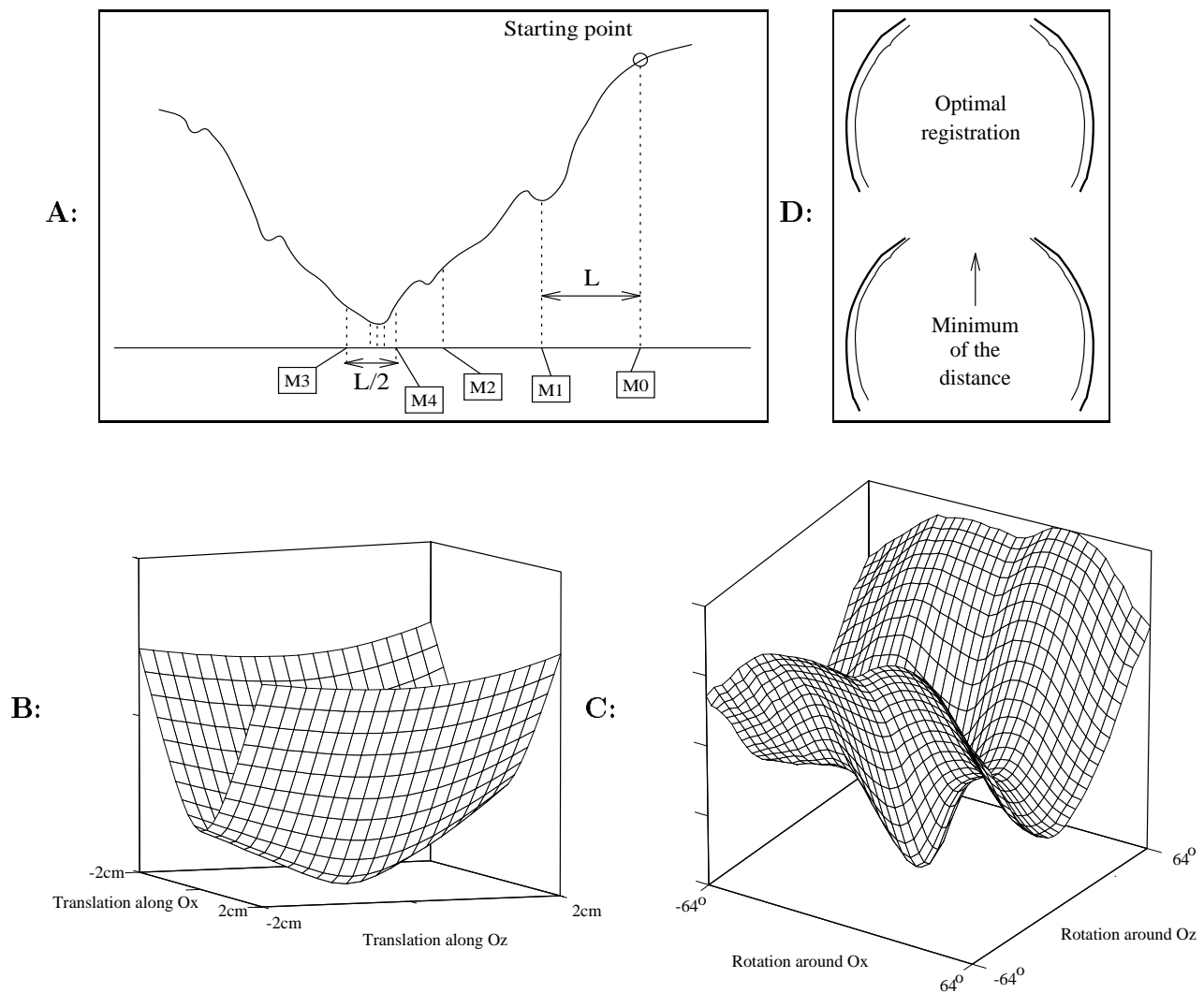


Figure 2: **A:** *Step by step minimization with a decreasing magnitude heuristic applied to a 1D function.*

The step magnitude is divided by two when the step by step algorithm has reached a minimum. The starting point is M_0 . The sequence M_0, M_1, M_2, M_3 corresponds to a downhill search with the initial step magnitude L . The next sequence M_3, M_4 corresponds to a step magnitude of $L/2$. The minimization ends when the step magnitude becomes lower than a preset threshold.

B: *Behaviour of the distance between both surfaces in function of the translation parameters:* the orientation of \mathcal{S}_{mob} is constant (10 degrees from the optimal orientation) and one of the three possible translations in the axe directions is fixed (the surface of interest is the head surface).

C: *Behaviour around the global minimum of the function measuring the fit for an orientation of \mathcal{S}_{mob} :* one of the three possible rotations around the axes is fixed; the fit is computed by associating to each orientation of \mathcal{S}_{mob} the translation which minimizes the distance between both surfaces (the surface of

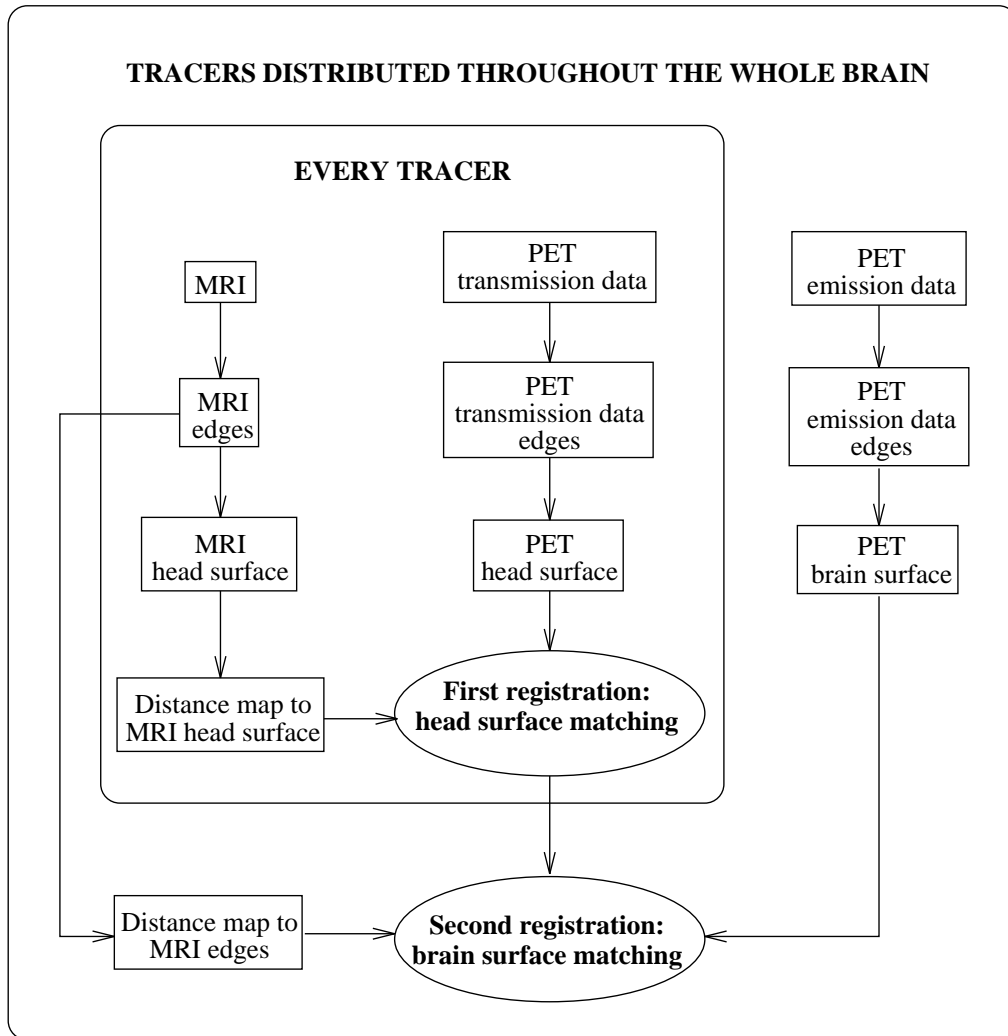


Figure 3: Nonsupervised algorithm for the PET/MRI 3-D registration.

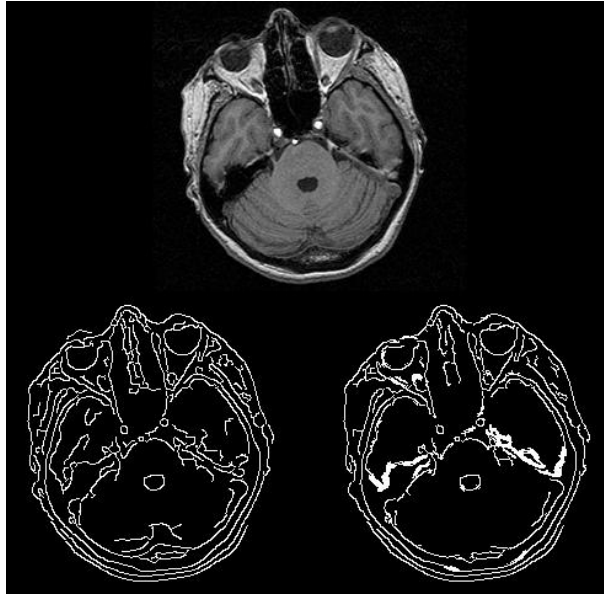


Figure 4: **2-D versus 3-D edge detection:**

top: original MRI slice;

bottom-left: 2-D edge detection;

bottom-right: 3-D edge detection.

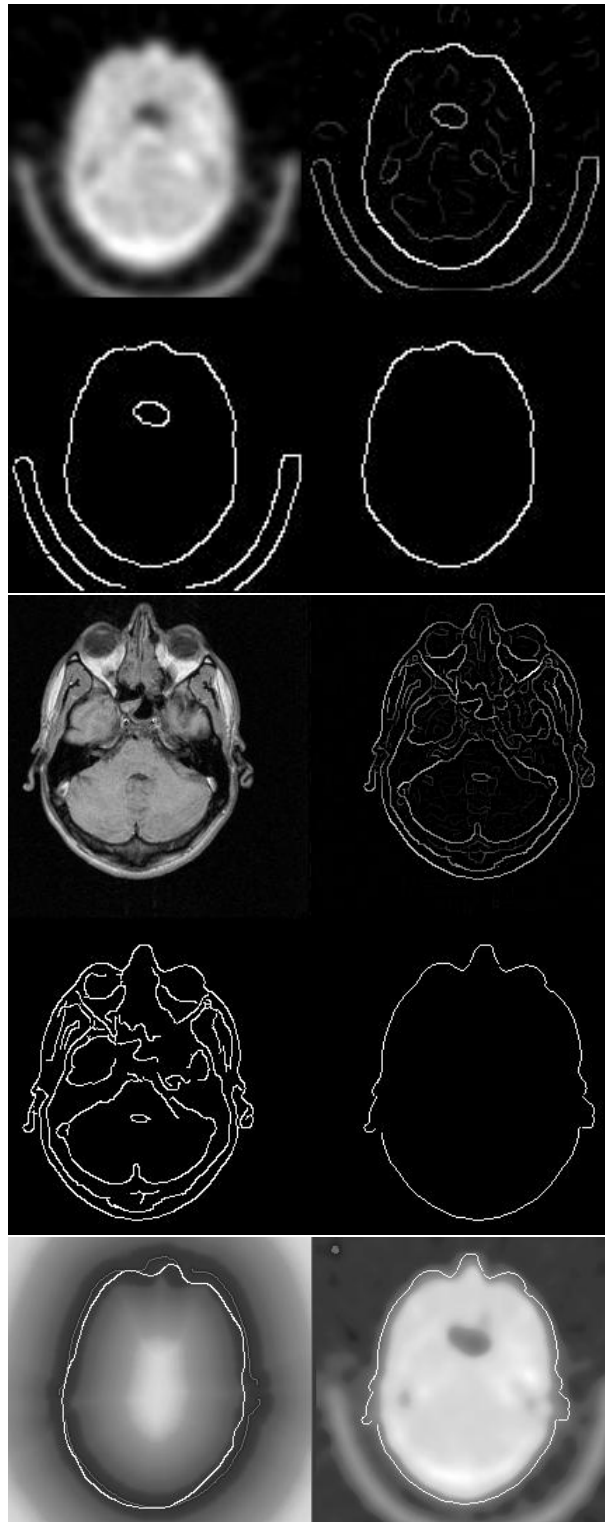


Figure 5: **First matching (head surface)**. Surface extraction in **(top)** PET transmission images and in **(middle)** MR images. For each modality: top-left: an original slice; top-right: 2-D Canny-Deriche filter; bottom-left: hysteresis thresholding; bottom-right: head surface. **Down:** left: a position of the mobile surface in the distance map during the matching; right: a PET transmission slice with the superimposed corresponding MRI edges after registration.

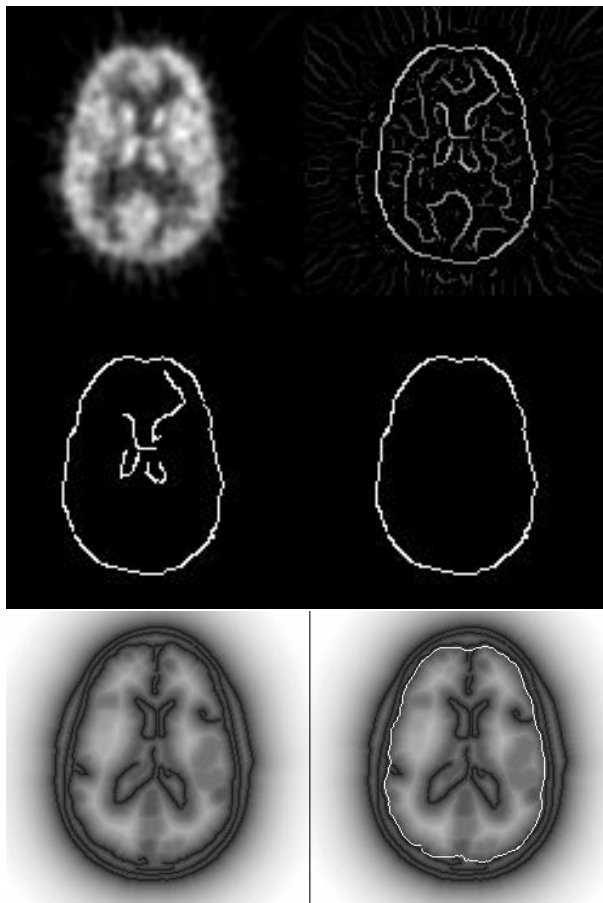


Figure 6: **Second matching (Brain surface)**. **Top:** Surface extraction in PET emission images: top-left: an original slice; top-right: 2-D Canny-Deriche filter; bottom-left: hysteresis thresholding; bottom-right: brain surface. **Down:** left: precomputation of a 3-D distance map to the MRI edges (axial view); right: a position of the mobile surface in the distance map during the matching.

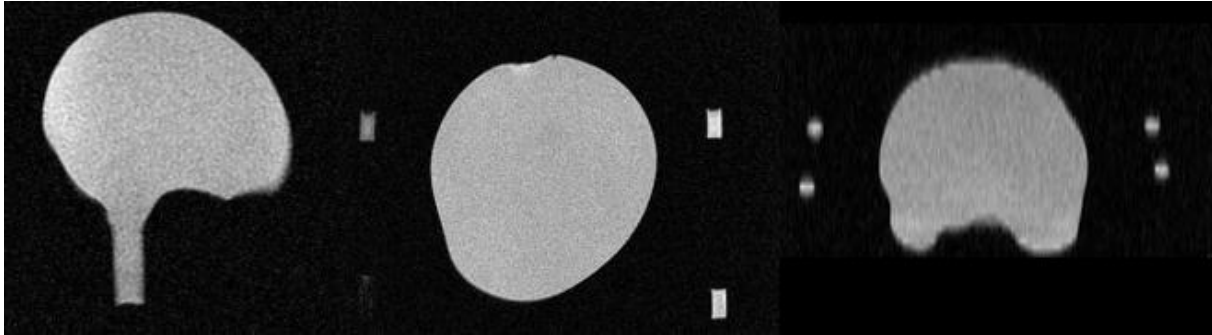


Figure 7: MR images of the rigid experimental device used for the validations (a brain-shaped phantom and 16 test tubes filled with ^{18}F). Left: sagittal view; middle: axial view; right: coronal view.

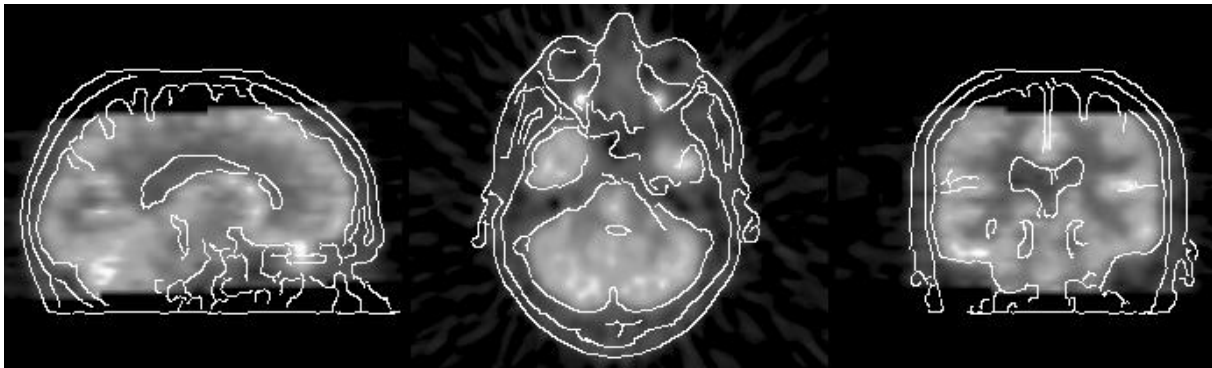


Figure 8: **Registration result with clinical data:** PET emission images (FDG) with the superimposed corresponding MRI edges after registration. Top: sagittal view; middle: axial view; bottom: coronal view.